

Determining the soil-bedrock interface and fracture-zone scope in the central urban area of the Jinan city, China, by using microtremor signals

Yanan Du^{1,2,3}, Peifen Xu^{1,2,3,*}, Suqun Ling⁴, Baoqing Tian^{1,2}, Zhiwei You^{1,2,3} and Ruohan Zhang^{1,2,3}

¹ Key Laboratory of Shale Gas and Geoengineering, CAS, Institute of Geology and Geophysics, Chinese Academy of Sciences, Beijing 100029, China

² Institutions of Earth Science, Chinese Academy of Sciences, Beijing 100029, China

³ University of Chinese Academy of Sciences, Beijing 100049, China

⁴ Geo-Analysis Institute Co., Ltd, Tokyo 184-00012, Japan

*Corresponding author: Peifen Xu. E-mail: pxu@mail.iggcas.ac.cn

Received 10 December 2018, revised 29 March 2019

Accepted for publication 19 April 2019

Abstract

To explore and utilize the urban underground space, it is important for us to accurately obtain information on the near surface structures. Microtremor signals play a vital role in that they carry abundant information about the subsurface structure and can be easily observed under disturbance of human activities in urban areas. We collected microtremor signals at 24 sites along a survey line in central Jinan city, obtained the dispersion curves by using the Extended Spatial Autocorrelation method and the resonance frequencies by using the horizontal-to-vertical spectral ratio method, and inverted the near surface structures by using the forking genetic algorithm. The lateral variation of the soil–rock interface was delineated at a maximum depth of 33 m and a large fracture zone was determined at a width of approximately 300 m. The frequency peaks changed from 2.5 to 7.3 Hz for the fracture and stable zones. A frequency-dependent model of the sediment thickness was obtained as $h = 101f_r^{-1.13}$, where h is the depth with a unit of m and f_r is the resonance frequency. These results may be useful for understanding near surface structures and then benefit exploration of urban underground space.

Keywords: microtremor signals, soil-bedrock interface, fracture-zone scope, nonlinear inversion, Jinan City

1. Introduction

Information about subsurface structure, such as overburden thickness, the geometry of the bedrock surface and the feature of the fracture zone, is key parameters for urban underground space utilization, city planning, civil engineering and environmental work. The variation of V_s directly reflects the change in lithology (Mainsant *et al.* 2012) since V_s is closely related to the dynamic properties of soil and rock such as the dynamic shear modulus and standard penetration test value (Anbazhagan *et al.* 2013). Therefore, information

regarding the soil–bedrock interface and fracture structure can be extracted by analyzing the subsurface V_s profile.

Different seismic methods can be used to estimate the subsurface V_s structure, ranging from invasive tests, including cross-hole, down-hole, up-hole and P-S suspension logging, to non-invasive tests including passive and active-source seismic methods such as the microtremor survey method, seismic refraction and seismic reflection. Nevertheless, the invasive tests suffer from several limitations that include difficulty in carrying out measurements in urban areas and the shortcomings of being time-consuming and expensive

due to the drilling involved (Rosa-Cintas *et al.* 2017). In view of this, non-invasive and cost-effective seismic methods have gained widespread acceptance as powerful tools in detecting information about the subsurface structure (Foti *et al.* 2018).

Due to the serious noise interference in an urban environment, it is hard to carry out geophysical exploration by using active-source seismic methods. On the contrary, the microtremor survey method can overcome these restrictions by taking advantage of the high level of ambient noise, which has gained wide applications such as in mapping deeply buried geothermal faults (Xu *et al.* 2012; Tian *et al.* 2016, 2017), investigating the strata structure of landslides (Du *et al.* 2018), seismic microzonation (Bonney-Claudet *et al.* 2009) and liquefaction evaluation (Rezaei & Choobbasti 2014).

One of the most commonly used methods is the single-station horizontal-to-vertical spectral ratio (HVSr) method. Due to its easy-implementation and low-cost, the HVSr method has been widely adopted in the field of site-effect assessment (Molnar *et al.* 2018; Vantassel *et al.* 2018) to determine the resonance frequency (f_r) of the subsoil. Variation of the resonance frequency is directly related to the geometry of soil–bedrock interface (Parolai *et al.* 2002), making it possible to reveal blind faults (Hellel *et al.* 2012). Moreover, the ability of the HVSr method to delineate bedrock geometry as a fast and economical geophysical exploration tool (Ibs-von Seht & Wohlenberg 1999; Parolai *et al.* 2002) has been tested. This method uses the empirical relationship between h and f_r , which is given by $h = af_r^b$, where a and b are site-specific parameters, to calculate the overburden thickness.

Another common method is the array-processing method, which allows the extraction of a dispersion curve from the data of multiple sensor records, and then the V_s profile by inversion. There are two main kinds of array-processing method including the spatial autocorrelation method (SPAC) (Aki 1957; Okada 2003) and the frequency-wavenumber Spectral method (FK) (Capon 1969). The array configuration required in the SPAC method is circular, while the requirement in the FK method is more flexible. To overcome the shortcoming of the SPAC arithmetic, Ling (1994) proposed the extended spatial autocorrelation (ESAC) method, which makes it possible to deal with irregularly shaped arrays. It has been demonstrated that the ESAC method gives more accurate results than FK in the low-frequency range when using the same sized array (Ohori *et al.* 2002).

In this study, we conducted microtremor observations, combining the HVSr method and the ESAC method along the designated survey line across the fault of Mount Qianfo in the urban area of Jinan, provincial capital of Shandong. Single-station measurements were taken to estimate the resonance frequency. Moreover, array measurements were

carried out to determine the V_s profile. The objective of this study was to assess the ability of the single-station and array-based microtremor survey method to map the soil–bedrock interface and image the fracture zone in highly populated urban areas where serious interference exists.

2. Geology in the urban area of the Jinan city

The study area was in the alluvial-diluvial piedmont plain, lying in the central urban area of Jinan, capital of east China's Shandong province (figure 1). The base consists of Paleozoic Ordovician carbonate rocks and magmatic intrusive rocks of the Yanshanian Stage with depths ranging from outcropping to >40 m (Song *et al.* 2016). According to the results of the available PS log, compared with carbonate rocks, the V_s values of the intrusive rocks are relatively low, and they are seriously weathered because of the long-term effects of environmental conditions. The soil deposits (all unconsolidated materials) overlying the bedrock are mainly man-made fill, silt clays and gravels ranging from a few meters to more than 30 m in thickness. The fault of Mount Qianfo is an important buried fault, the strike of which exhibits wave-shaped bending on the plane. Generally, the fault is oriented toward northwest-southeast and the width is from tens of meters to hundreds of meters (Song *et al.* 2016). The fault is widely covered by Quaternary sediments after entering the urban district of Jinan; therefore, knowledge of the precise localization of the fault is needed for this densely populated area.

3. Data and methods

3.1. Data acquisition

The equipment used to perform the measurements consists of a set of standalone three-channel 24-bit A/D digital datalogger (LS8800, manufactured by the Hakusan Corporation) connected to a triaxial velocity sensor (CDJ-SC2, manufactured by CGE (Chongqing) Geological Instrument Co., Ltd) with a natural frequency of 2 Hz. Adopting such a three-component seismic sensor makes it possible to acquire three components of microtremor data when performing array measurements, allowing for the extraction of supplementary information by using the HVSr data.

In total, 24 array measurements were taken with a separation of about 40 m between each site along the survey line across the fault of Mount Qianfo (figure 1). All measurements were performed by using a nested triangular array configuration. As shown in figure 2, 10 sensors were required for such a configuration, with one sensor (S_1) placed on the center and the other nine sensors (S_1 – S_{10}) equally distributed along the circumference of three circles forming three equilateral nested triangles. These three circles had the same center and the radii of these circles were 0.9, 10 and 20 m,

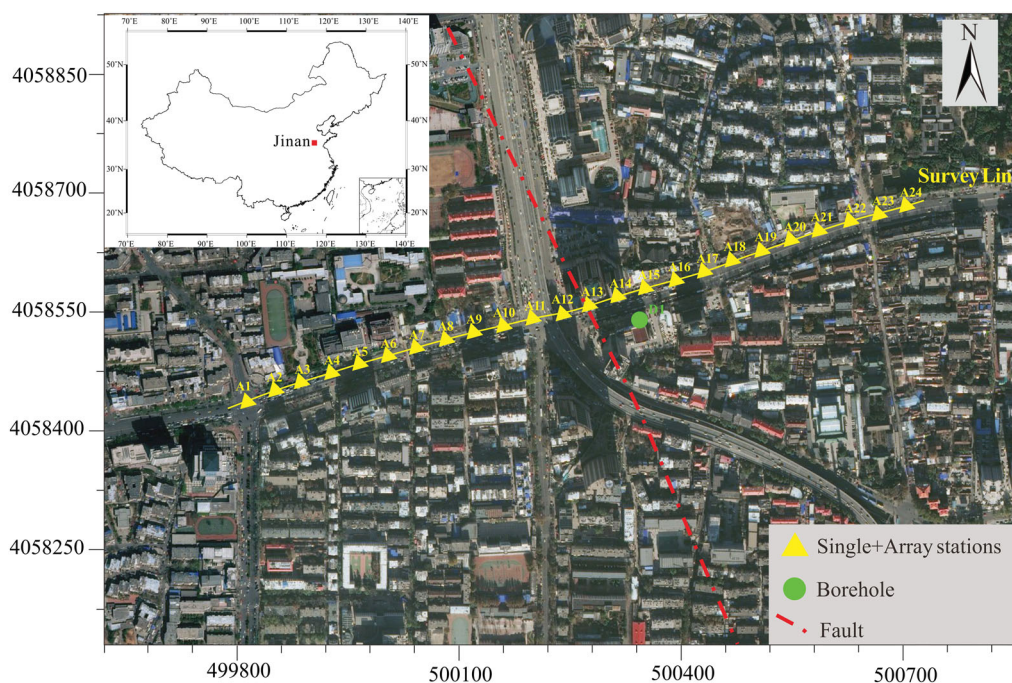


Figure 1. Map of the survey area located in the central urban area. Yellow triangles are the survey sites in this study, the borehole is represented by a green circle and the approximate position of the fault of Mount Qianfo is schematic marked by the dash-dotted line.

respectively. The inclusion of such a miniature array with a radius of 0.9 m can broaden the possible frequency band (Cho *et al* 2013), which is necessary to improve the precision of exploration.

After checking the synchronization of all recorders, simultaneous observations were made for 16 minutes at each site with the sampling interval being set to 0.01 s. Since all the survey points were in the central urban area, measurements were taken between 11 pm and 5 am local time to reduce the effects of local interference sources, with sensors directly placed on the asphalt pavement.

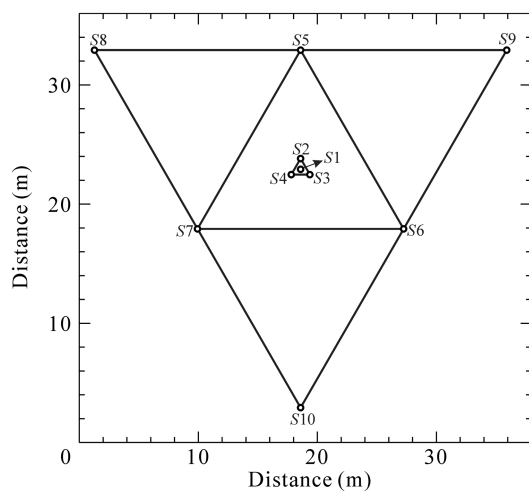


Figure 2. A schematic diagram of the array configuration.

3.2. Single-station analysis

The three components' microtremor signals were processed using the open-source Geopsy package (www.geopsy.org) to obtain the HVSR curve and then determine the resonance frequency. Before processing, windows of 20.48 s with the most stationary signals were selected automatically using an STA/LTA anti-trigger algorithm (Lee & Stewart 1981), which eliminated transients usually associated with anthropogenic noise. We calculated the Fourier amplitude spectra of the three components (including a 5% cosine taper applied to both ends of the non-overlapping windows) and smoothed them using a Konno and Ohmachi filter (Konno & Ohmachi 1998) with a constant of 40. Then, two horizontal components were merged by using the squared average and the HVSR was calculated by dividing the merged horizontal component spectrum by the vertical component spectrum. Finally, a mean HVSR curve was obtained by averaging the HVSR from all the analyzed windows.

To ensure the effectiveness of the results of each site, it was necessary to inspect the raw spectra of the three components signal to differentiate the HVSR peaks of stratigraphic origin from the HVSR peaks of anthropic origin. If all three components exhibit local narrow peaks, the HVSR peaks are likely from industrial origins, which may be related to some kinds of machinery, so then we should treat the results with caution (Castellaro 2016). Figure 3 parts a and c illustrate examples of HVSR curves for two sites and clear peaks around 5.8 and 2.7 Hz are observed, respectively. The curves of Fourier

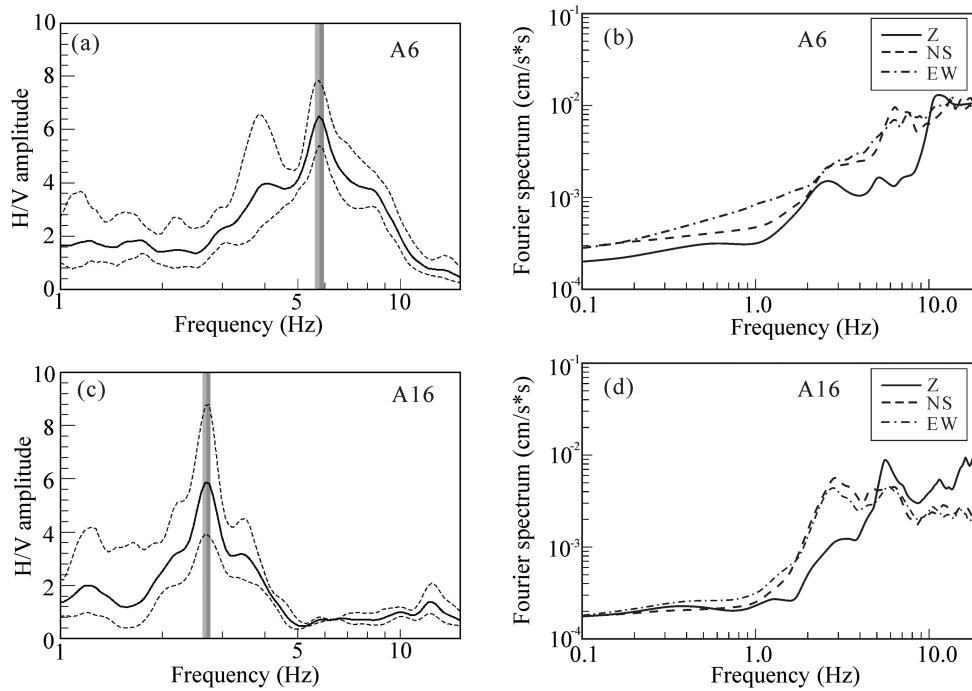


Figure 3. Left: (a) and (c) panels; average HVSr (thick line) and one standard deviation (dotted line) curves at site A6 and site A16. Right (b) and (d) panels; Fourier amplitude spectra of the three components at site A6 and site A16.

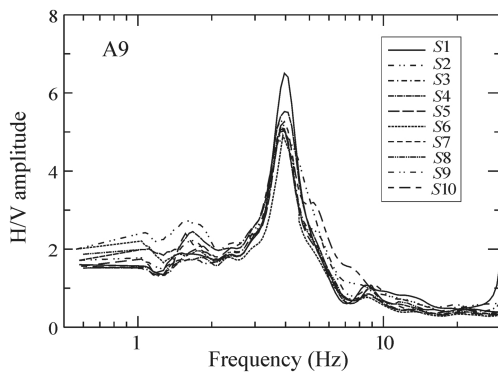


Figure 4. Variation of the HVSr curves for all sensors of the array for site A9.

amplitude spectra of three components for these two sites are shown in figure 3b and d.

3.3. Array analysis

Before processing, we tested the variation of the HVSr curves along the array to check whether the assumption that the layers under the array are approximately parallel, isotropic and homogeneous was met. Figure 4 shows the HVSr curves for all sensors of the array for site A9. In this case, these HVSr curves were characterized by a predominant peak at around 3.9 Hz and generally comparable with each other, indicating the 1D hypothesis was validated.

For simplicity, we termed an array with a radius of 0.9 m as miniature and with 10 and 20 m as large. We deal with

Table 1. The combination of two stations and its distance.

Type of array	Separation distance (m)	Station to station
Miniature array	0.9	S1–S2 S1–S3 S1–S4
	1.56	S2–S3 S2–S4 S3–S4
Large array	10.0	S1–S5 S1–S6 S1–S7
	17.3	S5–S6 S6–S7 S5–S7
	20.0	S1–S8 S1–S9 S1–S10
	30.0	S5–S10 S7–S9 S6–S8
	34.6	S8–S10 S8–S9 S8–S10

these measurements recorded by these two kinds of array separately.

Microtremor records of the vertical component were divided into time windows of 10.24 s for the miniature array and 20.24 s for the large array, with each window overlapped by half and tapered for 5% of its length using the cosine window to reduce any leakage effect (Carter et al. 1973). We discarded those windows with the abnormally large or small amplitudes and then calculated the power or cross spectrum of each window and smoothed using a Parzen window with a width of 0.3 Hz. As shown in the Table 1, there were two types of separation for the miniature array and five for the large array. The normalized autocorrelation functions of each station pair and the autocorrelation coefficients of each separation were calculated, respectively. Subsequently, two individual fittings between the autocorrelation coefficients of two arrays and the Bessel function of the zero-order first kind were performed to obtain the dispersion curves of the

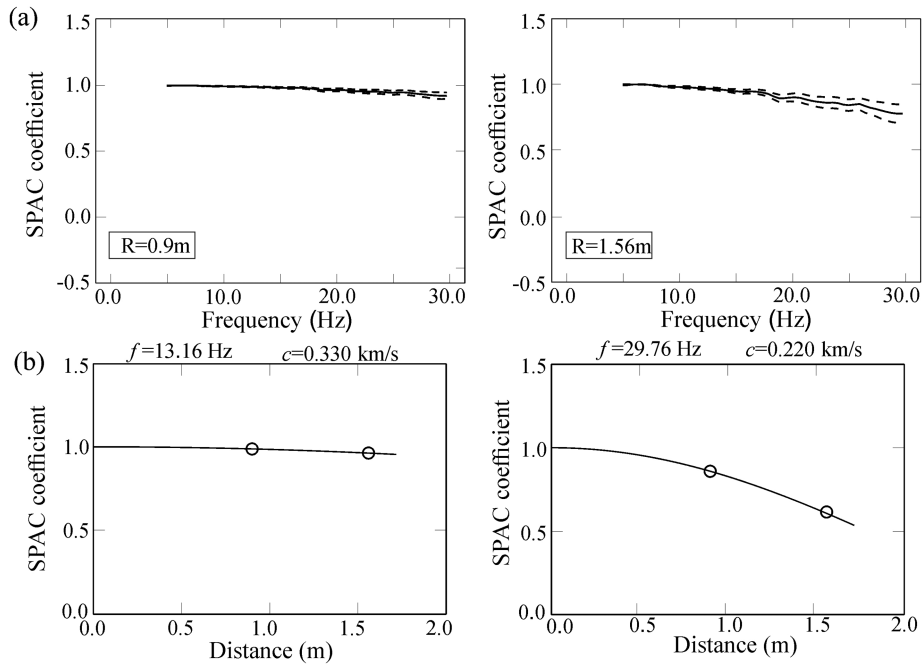


Figure 5. Results of microtremor data process for miniature array at site A9. (a) Solid lines represent average spatial autocorrelation coefficient curves, lower and upper dashed lines indicate upper and lower bound of standard deviation. (b) Examples of phase velocity of a Rayleigh wave fitted by the Bessel function for some frequencies (13.16 and 29.76 Hz). The solid lines show the Bessel function and circles represent the observed autocorrelation coefficient.

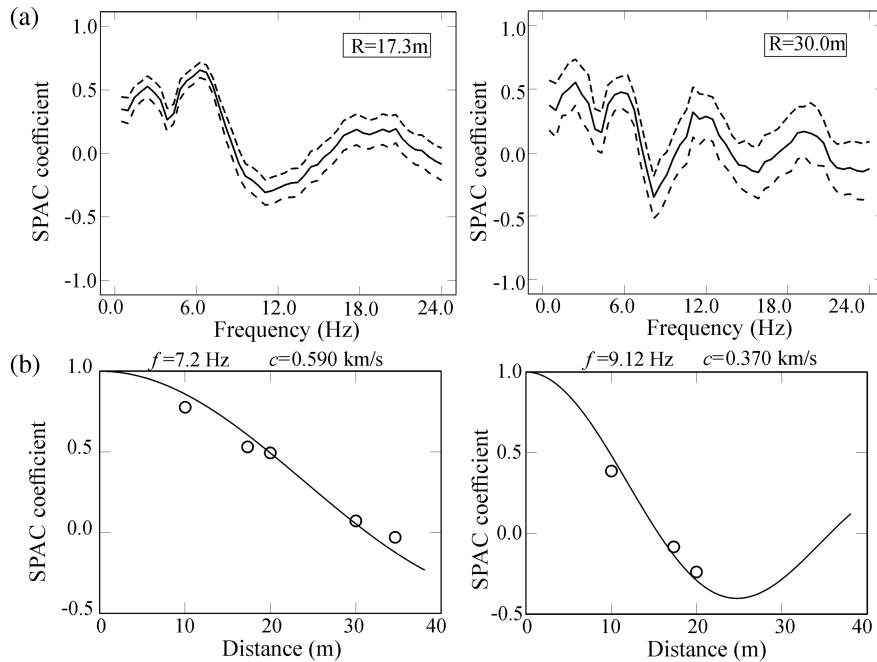


Figure 6. Results of microtremor data processing for the large array at site A9 (same legend as for figure 5).

Rayleigh wave. Finally, a combination of these two dispersion curves was conducted to determine the dispersion curve over a broad frequency band.

Figures 5 and 6 illustrate an example of microtremor data processing at site A9 with figures 5a and 6a showing the autocorrelation coefficients for the miniature and large array,

respectively, and figures 5b and 6b showing the phase velocity of a Rayleigh wave fitted by a Bessel function for four frequencies. In figure 6a, there was a decrease in autocorrelation coefficient below 6 Hz. Contrary to the expected value that autocorrelation coefficient will go infinitely close to 1 with a decrease of frequency and increase of phase velocity. This

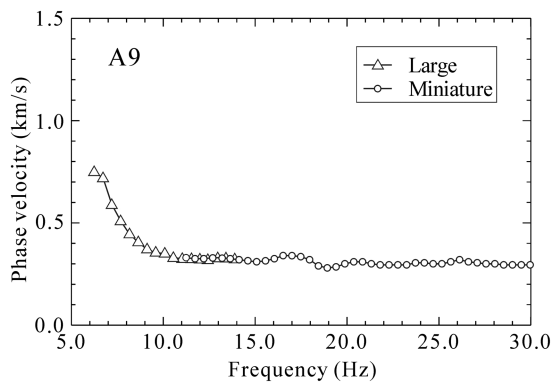


Figure 7. Comparison of dispersion curves inferred from the large and miniature array at the site A9.

kind of decrease was observed in other studies when using microtremor signals because of the limited maximum separation in the array (Asten et al. 2014). To get reliable results, we omitted the unreliable data below 6 Hz. Figure 7 shows the comparison of dispersion curves estimated from the miniature and large array. It is observed that the dispersion curve derived from the large array agrees well with that from the miniature array at the overlapping frequency. Therefore, it is possible to obtain a reliable dispersion curve for the frequency range of 6.24–30.24 Hz. The maximum wavelength is 119 m. As a rule of thumb, the investigation depth is about half of the maximum wavelength (Park et al. 1999); thus, its penetration depth would be 60 m.

The same procedure was applied to all other sites. The observed dispersion curves in figure 8 show differences from site to site. The phase velocities were derived at the frequency range of 10–30 Hz in sites A1–A11 and A20–A24, while we could acquire the phase velocities down to a lower frequency of 4.8 Hz in sites A12–A19. Over the frequency range 8–13 Hz, the phase velocities of sites A1–A11 and A20–A24 were much faster than those in sites A12–A19, presumably covered by thinner soil deposits.

3.4. Inversion

A global optimizing technique known as the forking genetic algorithm (fGA; Cho et al. 1999) was used to invert the observed phase velocities to find the appropriate 1D V_s profile. Sensitivity analysis (Xia et al. 1999) has shown that P-wave velocity (V_p) and density (ρ) have little effect on a dispersion curve. For this reason, during the inversion, the V_s and thickness of each layer were allowed to vary over pre-defined ranges, while the V_p and ρ were decided using the relationships from Kitsunezaki et al. (1990) $V_p = 1.1 * V_s + 1.29$ and Herrmann (2013) $\rho = 0.8 * \log(V_s) + 2.3$ (Herrmann 2013), respectively. Theoretical phase velocities of the fundamental mode were computed based on Haskell (1953). The search areas for the inversion were determined based on the borehole information and the values of V_s for each lithotype identified in the borehole were selected according to the literature data (Foti et al. 2018). After trial and error, we chose three or

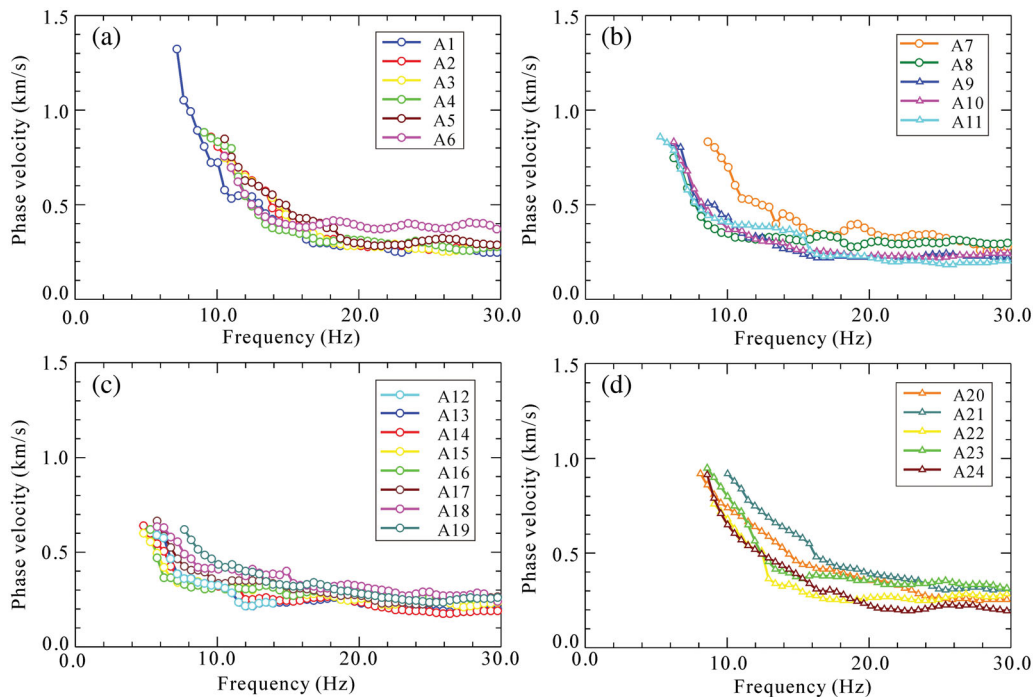


Figure 8. The observed dispersion curves of the Rayleigh wave for all sites.

Table 2. Parameter spaces for an inversion considering three or four layers.

Layer number	Three layers		Four layers	
	Thickness (m)	V_s (km s ⁻¹)	Thickness (m)	V_s (km s ⁻¹)
1	2–10	0.18–0.40	2–10	0.18–0.40
2	2–20	0.30–0.60	2–15	0.25–0.50
3	—	0.60–2.00	5–20	0.30–0.60
4	—	—	—	0.60–2.00

four layers in the inversion. In Table 2, the parameter spaces applied in the inversion were presented. The inversion was performed aiming to minimize the differences between the observed and theoretical phase velocities. The misfit function of the observed and theoretical phase velocities was defined as:

$$Misfit = \frac{1}{N} \sum \left[\frac{C_o(f) - C_t(f)}{C_o(f)} \right]^2$$

where N is the number of phase velocities, and $C_o(f)$ and $C_t(f)$ are observed and theoretical phase velocities.

Assuming the predominance of the fundamental mode of Rayleigh wave, six inversions with 6000 models generated in one inversion were conducted, and then the model with the smallest residuals among six estimations was chosen as final V_s profile. Figure 9a shows the comparison between observed and theoretical dispersion curves calculated from the best-fitting model for site A2 and it can be seen that both curves accord well with each other, indicating that the inverted model was acceptable. This is also proved by the decreasing trend of misfit value with the increase of generation number (figure 9b). It is evident that the misfit value began to drop rapidly and then gradually stabilized indicating the value convergence toward the global minimum.

4. Results and discussions

We calculated the HVSR using single-station measurements before the analysis of array-based records. The results offer a first idea about the geometry of the soil–bedrock interface, which is closely linked to the resultant HVSR resonance frequencies. The variation of the f_r along the survey line is depicted in figure 11a. It is clear that the f_r values change between 2.52 and 7.25 Hz. Since the bedrock depth h varies inversely with f_r , with the average V_s of the soil deposits being constant (Parolai et al. 2002), f_r is characterized by a smaller value where the regions have thick soil deposits that are probably related to the fracture zone. At each side of the survey line, the significant increases in f_r values reveal important basement uplift over a small distance of 40 m or less. One possible explanation for this uplift is a cluster of two sub-order faults accompanied by the main fault.

After HVSR analysis, the ESAC method was applied to extract dispersion curves from array measurements, and then the subsurface V_s structures of each site can be acquired by adopting an fGA method for the inversion. Figure 10 shows a comparison between the inverted V_s profiles of sites in zones 1 and 2 located on the stable zone and sites in the fracture zone. Such a set of 1D V_s profiles has been interpolated using the Kriging method (Pokhrel et al. 2013) to generate a 2D V_s map (figure 11b) along the survey line. The information from borehole D1 (see figure 1 for relative location) was used to correlate the V_s map with the geological structure. The section that was divided into three zones (zone 1, fracture zone and zone 2) based on the characteristics of V_s profiles, was interpreted as follows:

The fracture zone has a V_s of 150–350 m s⁻¹ in the top 6–10 m, corresponding to miscellaneous fill and silt clay. The next 20–25 m shows a V_s of 350–500 m s⁻¹, which is related to gravel clay. A total soil thickness, of which V_s values are lower than 760 m s⁻¹ (Anbazhagan & Sitharam 2009), is approximately 25–35 m. The engineering bedrock with V_s of 800–1000 m s⁻¹ is located at the bottom, the geological

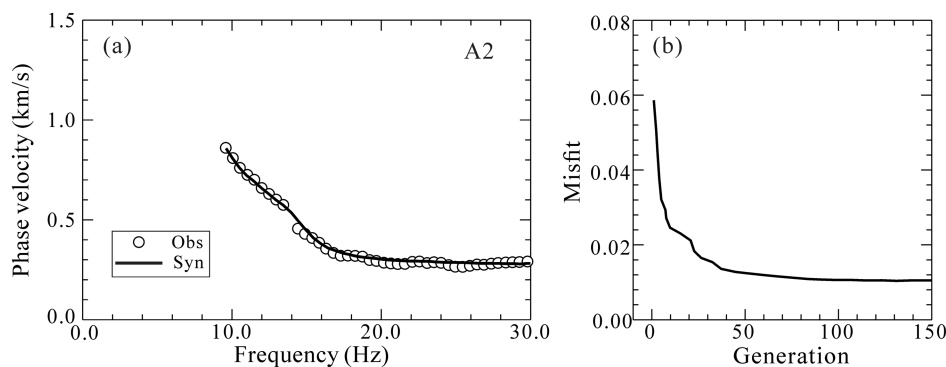


Figure 9. (a) Comparison between observed (circle) and best-fitting theoretical (solid line) phase velocities for site A2 and (b) misfit value as a function of generation.

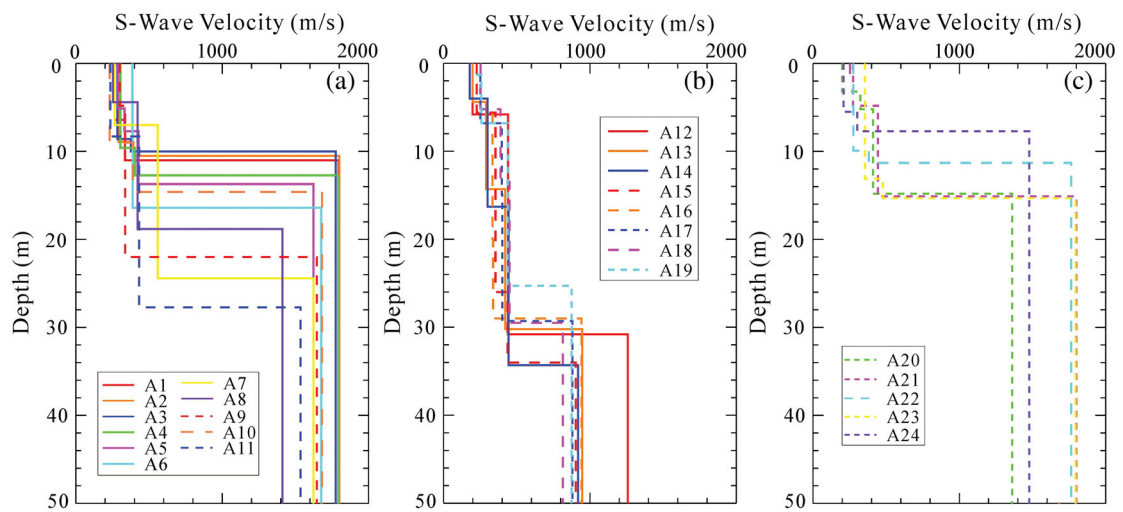


Figure 10. Comparison of the inverted V_s profiles. (a) sites in zone 1 located in the stable zone. (b) sites in the fracture zone. (c) sites in zone 2 located in the stable zone.

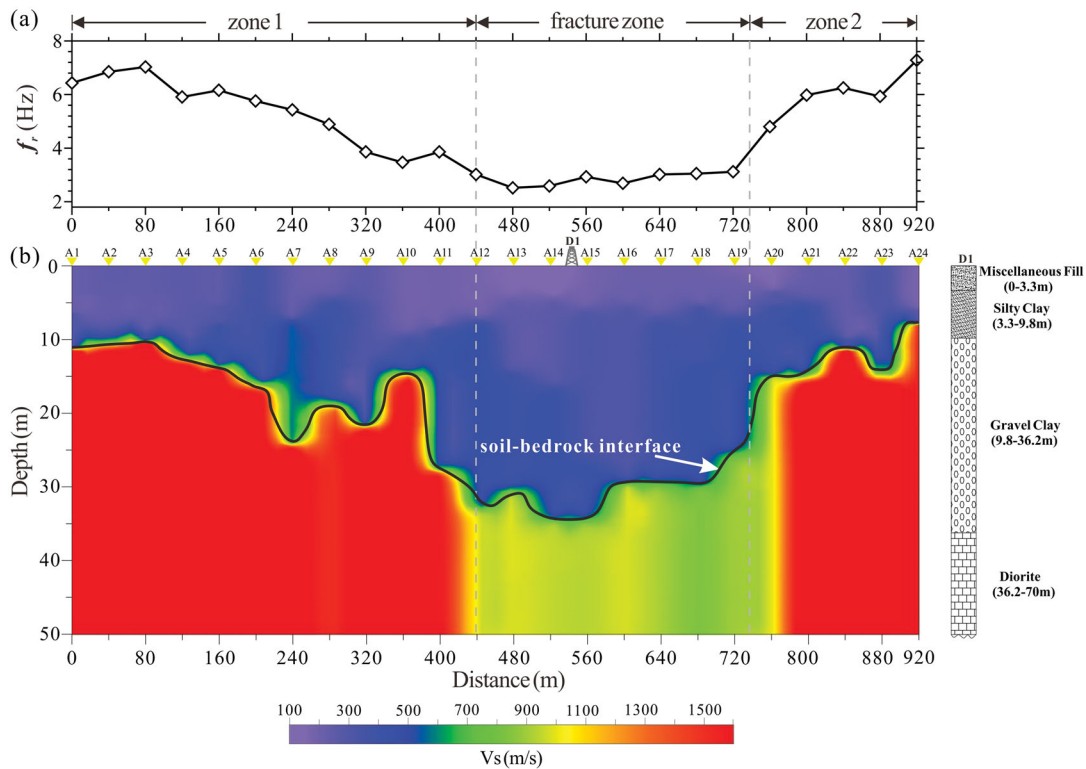


Figure 11. (a) Variation of the resonance frequency along the survey line. (b) The V_s map along the survey line from array results. Yellow triangles indicate the projection of the measurement points. Borehole logs of D1 are shown in the right. The thick black line represents the interface of the soil and bedrock.

content of the layer was observed to be diorite and the intrusive rock was relatively broken and rich in water because of long-term weathering denudation.

Zones 1 and 2 have a more heterogeneous soil layer and the geological substances of the surface layers, of which $V_s < 760 \text{ m s}^{-1}$, also consist of silt clay and gravel clay. The thickness of the soil layer changes rapidly, ranging from 8 to 23 m and displaying a dip to the middle of the section. The

layer with V_s values of $> 1300 \text{ m s}^{-1}$ was identified as engineering bedrock, of which the geological unit was Paleozoic Ordovician limestone. Compared with intrusive rock, the limestone was compacted, complete and possessed higher V_s , which is consistent with the results of the previous PS log.

According to those results, the interface of soil–bedrock can be delineated by the thick black line in figure 11b. It is clear that the soil-bedrock interface is not a geometric

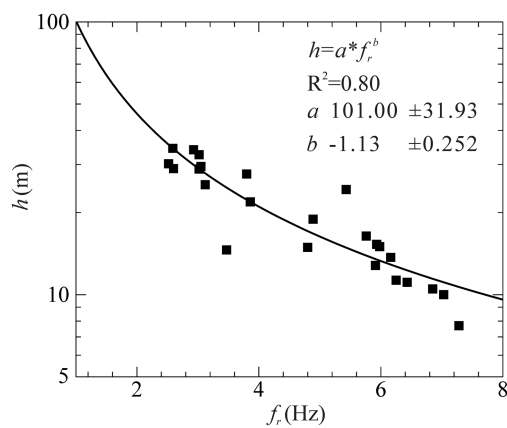


Figure 12. Sediment thickness as a function of the resonance frequency for 24 sites. The best fit values and R^2 are shown.

surface, but a rather undulating boundary with depth varying from 8 to 35 m. Rapid subsidence and uplift of bedrock can be observed in the ranges of A11–A12 and A19–A20, respectively, probably due to the existence of two secondary faults. The width of the fracture zone was roughly 300 m, which was consistent with the results of previous studies (Song *et al.* 2016).

The empirical relationship between the thickness h of the sedimentary layer computed from the inversion of Rayleigh wave and the resonance frequency f_r calculated from the HVSR data was developed. The plot of the thickness h of the sedimentary layer as a function of the resonance frequency f_r is shown in figure 12 and the values of best fit parameters a and b equal to 101 and -1.132 , respectively. The errors of a and b for confidence of 95% are ± 31.93 and ± 0.252 , respectively.

Finally, theoretical 1D SH transfer functions were calculated using the 1D propagator-matrix by Haskell (1953) for all the models in figure 10. For this modeling, we assumed the Q value of each layer to be 1/15 of its V_s (Iida *et al.* 2005). A comparison between the peak of theoretical 1D SH transfer function and peak of the observed HVSR curve was made to validate the resultant model (figure 13). From the large R^2 , it is clear that HVSR peak frequencies were generally in agreement with those of the transfer function, indicating the inversion results were reliable (Bonnetfoy-Claudet *et al.* 2008).

5. Conclusion

In this study, in order to map the soil–bedrock interface and identify the position and width of the fracture zone, we carried out single-station and array microtremor measurements at 24 sites along the survey line in the urban area of Jinan. Our goal was to use the HVSR method to determine the resonance frequency, and the ESAC method to extract the dispersion curves and then to derive V_s profiles.

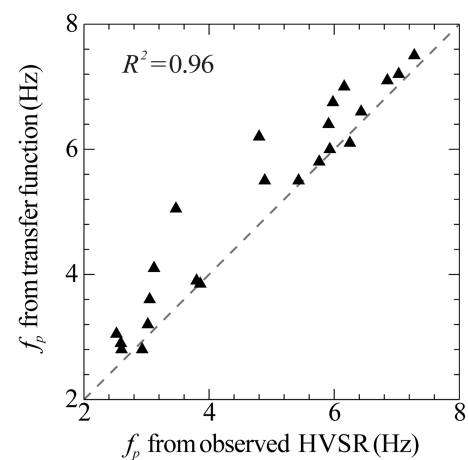


Figure 13. Comparison of the peak frequency from transfer function and HVSR data.

The results show the fracture zone exhibited low V_s and f_r , whereas high V_s and f_r were found in the stable zone. The geometry of the top of the basement was delineated, the depth of which showed rapidly spatial variation ranging from 8 to 35 m. Rapid subsidence and uplift of bedrock occurred over a small distance of 40 m or less, probably affected by two secondary faults and the V_s map reveals a comparably large fracture zone with a width of approximately 300 m. The nonlinear regression relation between the resonance frequency f_r (Hz) and the sediment thickness h (m) for Jinan City is derived as $h = 101f_r^{-1.132}$, which could be useful in engineering application. Finally, to verify the reliability of the V_s profile obtained from array measurements, the peak frequency of HVSR curve was compared with that of the transfer function for the modeled V_s profile. A good agreement between them showed that ESAC modeling results were reliable.

Acknowledgements

This work has been funded by The China Geological Survey Bureau under the Geological Survey Project (No. DD20179611) and National Natural Science Foundation of China (No. 41474044).

Conflict of interest statement. None declared.

References

- Aki, K., 1957. Space and time spectra of stationary stochastic waves, with special reference to microtremors, *Bulletin of the Earthquake Research Institute*, **35**, 415–456.
- Anbazhagan, P., Kumar, A. & Sitharam, T.G., 2013. Seismic site classification and correlation between standard penetration test N value and shear wave velocity for Lucknow City in Indo–Gangetic Basin, *Pure and Applied Geophysics*, **170**, 299–318.
- Anbazhagan, P. & Sitharam, T.G., 2009. Spatial variability of the depth of weathered and engineering bedrock using multichannel analysis of surface wave method, *Pure and Applied Geophysics*, **166**, 409–428.

- Asten, M.W., Askan, A., Ekincioglu, E.E., Sisman, F.N. & Ugruhan, B., 2014. Site characterisation in north-western Turkey based on SPAC and HVSR analysis of microtremor noise, *Exploration Geophysics*, **45**, 74–85.
- Bonnefoy-Claudet, S., Baize, S., Bonilla, L.F., Berge-Thierry, C., Pasten, C., Campos, J. & Verdugo, R., 2009. Site effect evaluation in the basin of Santiago de Chile using ambient noise measurements, *Geophysical Journal International*, **176**, 925–937.
- Bonnefoy-Claudet, S., Köhler, A., Cornou, C., Wathelet, M. & Bard, P.Y., 2008. Effects of Love waves on microtremor H/V ratio, *Bulletin of the Seismological Society of America*, **98**, 288–300.
- Capon, J., 1969. High-resolution frequency-wavenumber spectrum analysis, *Proceedings of the IEEE*, **57**, 1408–1418.
- Carter, G.C., Knapp, C.H. & Nuttall, A.H., 1973. Estimation of the magnitude-squared coherence function via overlapped Fast Fourier Transform processing, *IEEE Transactions on Audio and Electroacoustics*, **21**, 337–344.
- Castellaro, S., 2016. The complementarity of H/V and dispersion curves, *Geophysics*, **81**, T323–T338.
- Cho, I., Nakanishi, I., Ling, S.Q. & Okada, H., 1999. Application of Forking Genetic Algorithm fGA to an exploration method using microtremors, *Geophysical Exploration (Butsuri-Tansa)*, **52**, 227–246.
- Cho, I., Senna, S. & Fujiwara, H., 2013. Miniature array analysis of microtremors, *Geophysics*, **78**, KS13–KS23.
- Du, Y.N., Xu, P.F. & Ling, S.Q., 2018. Microtremor survey of soil-rock mixture landslide: a case study of landslide in Baidian Township, Hengyang City, *Chinese Journal of Geophysics*, **61**, 1596–1604.
- Foti, S. et al., 2018. Guidelines for the good practice of surface wave analysis: a product of the InterPACIFIC project, *Bulletin of Earthquake Engineering*, **16**, 2367–2420.
- Haskell, N.A., 1953. The dispersion of surface waves on multilayered media, *Bulletin of the Seismological Society of America*, **43**, 17–34.
- Hellel, M., Oubaiche, E.H., Chatelain, J.L., Machane, D., Bensalem, R., Guillier, B. & Cheikhounis, G., 2012. Basement mapping with single-station and array ambient vibration data: delineating faults under Boumerdes City, Algeria, *Seismological Research Letters*, **83**, 798–805.
- Herrmann, R.B., 2013. Computer programs in seismology: an evolving tool for instruction and research, *Seismological Research Letters*, **84**, 1081–1088.
- Ibs-von Seht, M. & Wohlenberg, J., 1999. Microtremor measurements used to map thickness of soft sediments, *Bulletin of the Seismological Society of America*, **89**, 250–259.
- Iida, M., Yamanaka, H. & Yamada, N., 2005. Wave field estimated by borehole recordings in the reclaimed zone of Tokyo Bay, *Bulletin of the Seismological Society of America*, **95**, 1101–1119.
- Kitsunezaki, C., Goto, N., Kobayashi, Y., Ikawa, T., Horike, M., Saito, T., Kurota, T., Yamane, K. & Okuzumi, K., 1990. Estimation of P and S wave velocities in deep soil deposits for evaluating ground vibrations in earthquake, *Journal of Japan Society for Natural Disaster Science*, **9**, 1–17.
- Konno, K. & Ohmachi, T., 1998. Ground-motion characteristics estimated from spectral ratio between horizontal and vertical components of microtremor, *Bulletin of the Seismological Society of America*, **88**, 228–241.
- Lee, W.H.K. & Stewart, S.W., 1981. *Principles and Applications of Microearthquake Networks*, Academic press.
- Ling, S.Q., 1994. Research on the estimation of phase velocities of surface waves in microtremors, *PhD thesis*, Hokkaido University, Japan.
- Mainsant, G., Jongmans, D., Chambon, G., Larose, E. & Baillet, L., 2012. Shear-wave velocity as an indicator for rheological changes in clay materials: lessons from laboratory experiments, *Geophysical Research Letters*, **39**, L19301.
- Molnar, S., Cassidy, J.F., Castellaro, S., Cornou, C., Crow, H., Hunter, J.A. & Yong, A., 2018. Application of microtremor horizontal-to-vertical spectral ratio (MHVSR) analysis for site characterization: state of the art, *Surveys in Geophysics*, **39**, 1–19.
- Ohuri, M., Nobata, A. & Wakamatsu, K., 2002. A comparison of ESAC and FK methods of estimating phase velocity using arbitrarily shaped microtremor arrays, *Bulletin of the Seismological Society of America*, **92**, 2323–2332.
- Okada, H., 2003. The microtremor survey method, *Geophysical Monograph Series 12*, SEG.
- Park, C.B., Miller, R.D. & Xia, J., 1999. Multichannel analysis of surface waves, *Geophysics*, **64**, 800–808.
- Parolai, S., Bormann, P. & Milkereit, C., 2002. New relationships between Vs, thickness of sediments, and resonance frequency calculated by the H/V ratio of seismic noise for the Cologne area (Germany), *Bulletin of the Seismological Society of America*, **92**, 2521–2527.
- Pokhrel, R.M., Kuwano, J. & Tachibana, S., 2013. A Kriging method of interpolation used to map liquefaction potential over alluvial ground, *Engineering Geology*, **152**, 26–37.
- Rezaei, S. & Choobbasti, A.J., 2014. Liquefaction assessment using microtremor measurement, conventional method and artificial neural network (case study: Babol, Iran), *Frontiers of Structural and Civil Engineering*, **8**, 292–307.
- Rosa-Cintas, S., Clavero, D., Delgado, J., López-Casado, C., Galiana-Merino, J.J. & Garrido, J., 2017. Characterization of the shear wave velocity in the metropolitan area of Málaga (S Spain) using the H/V technique, *Soil Dynamics and Earthquake Engineering*, **92**, 433–442.
- Song, W., Chen, S., Ge, F., Wu, Z. & Lv, C., 2016. The analysis of comprehensive geophysical detection and seismicity of fracture of Mount Qianfo, *Computerized Tomography Theory and Applications*, **25**, 523–530.
- Tian, B., Xu, P., Ling, S., Xu, X., Du, J. & Pang, Z., 2016. Application of the initial model feature of microtremor to investigate a part of the geothermal field of Jiangsu region in China, *Environmental Earth Sciences*, **75**, 1298.
- Tian, B., Xu, P., Ling, S., Du, J., Xu, X. & Pang, Z., 2017. Application effectiveness of the microtremor survey method in the exploration of geothermal resources, *Journal of Geophysics and Engineering*, **14**, 1283–1289.
- Vantassel, J., Cox, B., Wotherspoon, L. & Stolte, A., 2018. Mapping depth to bedrock, shear stiffness, and fundamental site period at CentrePort, Wellington, using surface-wave methods: implications for local seismic site amplification, *Bulletin of the Seismological Society of America*, **108**, 1709–1721.
- Xia, J., Miller, R.D. & Park, C.B., 1999. Estimation of near-surface shear-wave velocity by inversion of Rayleigh waves, *Geophysics*, **64**, 691–700.
- Xu, P., Ling, S., Li, C., Du, J., Zhang, D., Xu, X. & Zhang, Z., 2012. Mapping deeply-buried geothermal faults using microtremor array analysis, *Geophysical Journal International*, **188**, 115–122.